

Rolling velocity and relative motion of particle detector in local granular flow

Ran Li(李然), Bao-Lin Liu(刘宝林), Gang Zheng(郑刚), and Hui Yang(杨晖)

Citation: Chin. Phys. B, 2022, 31 (**11**): 114501. DOI: 10.1088/1674-1056/ac7dc0

What follows is a list of articles you may be interested in

Correlation mechanism between force chains and friction mechanism during powder compaction

Ning Zhang(张宁), Shuai Zhang(张帅), Jian-Jun Tan(谈健君), and Wei Zhang(张炜)

Chin. Phys. B, 2022, 31 (**2**): 024501. DOI: 10.1088/1674-1056/ac0db1

Three-dimensional clogging structures of granular spheres near hopper orifice

Jing Yang(杨敬), Dianjinfeng Gong(宫殿锦丰), Xiaoxue Wang(汪晓雪), Zhichao Wang(王志超), Jianqi Li(李建奇), Bingwen Hu(胡炳文), and Chengjie Xia(夏成杰)

Chin. Phys. B, 2022, 31 (**1**): 014501. DOI: 10.1088/1674-1056/ac2f2f

Parametric study of the clustering transition in vibration driven granular gas system

Qi-Lin Wu(吴麒麟), Mei-Ying Hou(厚美瑛), Lei Yang(杨磊), Wei Wang(王伟), Guang-Hui Yang(杨光辉), Ke-Wei Tao(陶科伟), Liang-Wen Chen(陈良文), Sheng Zhang(张晟)

Chin. Phys. B, 2020, 29 (**5**): 054502. DOI: 10.1088/1674-1056/ab8217

Experimental and numerical study on energy dissipation in freely cooling granular gases under microgravity

Wen-Guang Wang(王文广), Mei-Ying Hou(厚美瑛), Ke Chen(陈科), Pei-Dong Yu(虞培东), Matthias Sperl

Chin. Phys. B, 2018, 27 (**8**): 084501. DOI: 10.1088/1674-1056/27/8/084501

Decaying solitary waves propagating in one-dimensional damped granular chain

Zongbin Song(宋宗斌), Xueying Yang(杨雪滢), Wenxing Feng(封文星), Zhonghong Xi(席忠红), Liejuan Li(李烈娟), Yuren Shi(石玉仁)

Chin. Phys. B, 2018, 27 (**7**): 074501. DOI: 10.1088/1674-1056/27/7/074501

Rolling velocity and relative motion of particle detector in local granular flow

Ran Li(李然)[1,†], Bao-Lin Liu(刘宝林)[1], Gang Zheng(郑刚)[1], and Hui Yang(杨晖)[2,‡]

[1] *School of Health Science and Engineering, University of Shanghai for Science and Technology, Shanghai* 200093, *China*
[2] *School of Optical-Electrical and Computer Engineering, University of Shanghai for Science and Technology, Shanghai* 200093, *China*

(Received 9 May 2022; revised manuscript received 27 June 2022; accepted manuscript online 2 July 2022)

The velocity of a particle detector in granular flow can be regarded as the combination of rolling and sliding velocities. The study of the contribution of rolling velocity and sliding velocity provides a new explanation to the relative motion between the detector and the local granular flow. In this study, a spherical detector using embedded inertial navigation technology is placed in the chute granular flow to study the movement of the detector relative to the granular flow. It is shown by particle image velocimetry (PIV) that the velocity of chute granular flow conforms to Silbert's formula. And the velocity of the detector is greater than that of the granular flow around it. By decomposing the velocity into sliding and rolling velocity, it is indicated that the movement of the detector relative to the granular flow is mainly caused by rolling. The rolling detail shown by DEM simulation leads to two potential mechanisms based on the position and drive of the detector.

Keywords: local velocity distribution, rolling velocity, inertial navigation technology, relative velocity dependent (RVD) rolling friction

PACS: 45.70.–n, 45.70.Ht, 45.50.–j **DOI:** 10.1088/1674-1056/ac7dc0

1. Introduction

Traditional granular flow velocity distribution is studied usually[1] by using the monodisperse granular flow for the exploration of flow models[2,3] while the the research of polydisperse particle flow focuses on the mechanism of mixing and segregation.[4,5] However, there is a special particle flow of a few special particles worthy of attention in the nearly monodisperse granular flow, *e.g.*, rock landslides with accompanying debris flows are examples of such particle flows.[6] The number of special particles cannot form the statistical characteristics to support the segregation and mixing model exploration. The description of the movement of the special particles relative to the granular flow is very lacking. This process can be studied by placing inertial navigation detector into the chute granular flow, which can provide a valuable reference for the study of the movement process of special particles.

In the absence of a unified framework, granular flows in a chute are commonly divided into three different regimes based on the inertial number.[7] This study focuses on the viscous-like regime. The material flow is more like a liquid with a shear-rate-dependent stress under this regime.[8]

The local rheology is the most widely recognized mathematical model for viscous-like granular flow in an inclined chute.[9,10] Forterre and Pouliquen[11] and Tripathi and Khakha[12] summarized the local flow velocity distribution model as shown in Fig. 1(a). A granular layer of thickness h flows down a rough plane inclined at an angle $8^\circ < \theta < 12^\circ$. The force balance for steady uniform flows implies that the ratio between shear stress and normal stress is constant and equal to $\tan\theta$. Experimentally or numerically, the mean velocity varies as the power 3/2 of the depth and increases with inclination. The physical mechanism is the nonlinear correlation between the friction coefficient μ and the inertial number I[7,9] in the quasi static and kinetic regime, specifically

$$\mu(I) = \mu_s + \frac{\mu_2 - \mu_s}{I_0/I + 1}, \tag{1}$$

which is shown in Fig. 1(b).

However, this model does not distinguish between the velocity caused by particle sliding and that by particle rolling. The latest research shows that rolling has an important influence on the movement of granular flow.[13,14]

Wang *et al*. reported a study on the granular flow layers by using the embedded inertial navigation techniques.[15] This provides a new method of studying particle rolling in a particle flow. Caviezel *et al*. studied rockfall on Alps by using a detector equipped with a situ sensor, and successfully reconstructed the falling trajectory of the detector.[16,17] Zhu *et al*. improved the navigation techniques and applied them to the study of the funnel flow particle rolling in the laboratory, and accurately measured the angular velocity distribution of the tracer particles in the funnel flow.[18] It was found that there is a close relationship between rolling and the granular flow velocity distribution. This provides an important reference for the study of the relative particle flow motion of special particles.

[†]Corresponding author. E-mail: ran89@usst.edu.cn
[‡]Corresponding author. E-mail: Yanghui@usst.edu.cn

© 2022 Chinese Physical Society and IOP Publishing Ltd

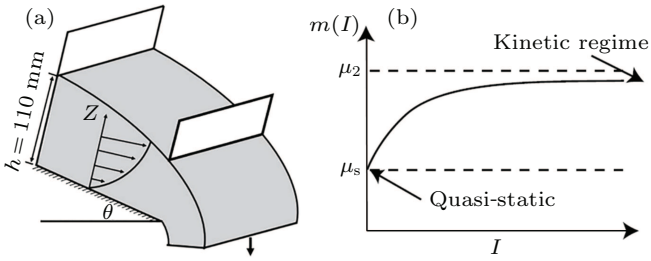


Fig. 1. Local flow velocity distribution in chute granular flow: (a) schematic diagram of flat inclined chute and (b) nonlinear correlation between friction coefficient and inertial number.[11,12]

It should be noted that the PIV method and the x-ray method will not interfere with the particle flow and are a reliable method to measure the particle flow velocity distribution.[19] Since x-ray may offset the inertial navigation device, the PIV is chosen to measure the velocity distribution of chute granular flow which is used as the baseline. However, there are physical parameters which cannot be obtained by the experimental technology. With the development of computer technology, the discrete element method (DEM) is increasingly used in the granular flow mechanism research field.[20,21] The DEM can track the real-time motion of each particle, and obtain the particle's rotational motion information.[22] The influence of rolling friction coefficient was investigated in Yu and Saxen's DEM study of Silo.[23] Tripathi *et al*. adopted the relative velocity dependent (RVD) rolling friction in quantitative DEM simulation of non-spherical particle.[24] Taking the rolling friction into consideration in the model, the consistency of simulation results and experimental results is improved.

In this work, the data obtained from DEM simulation validated by spherical detector experiments are used to study the local granular flow, attempting to identify the velocity of particle as the rolling and sliding velocity in local flow velocity so as to provide a new perspective for the study of the movement of special particles relative to granular flow.

2. Experimental setups

2.1. Chute granular flow

Based on the theoretical model, the experimental process in this study can be seen in Fig. 2. The chute granular flow lasted 2.7 s on average and 2.8 s in this experiment served as an example. At $t_0 = 0$, the baffle is removed and the particles started to move. The velocity distribution is unstable initially but at $t_1 = 0.6$ s, the chute granular flow forms a stable local flow velocity distribution. After $t_2 = 1.2$ s, owing to the inadequate thickness of the particle bed in the chute, the local flow velocity distribution cannot be maintained.

We use the PIV technique to obtain the velocity on the side wall of the chute, as shown in Fig. 2(d). The detector is used as the special particle of concern (diameter of 30 mm), surrounded by small particles (diameter of 10 mm) inside the chute. The spherical detector can obtain the particle's acceleration and rotation angular velocity. Therefore, the particle velocities of different initial heights in the chute and the composition of particle velocity under different inclination angles are studied. The position of the spherical detector is Z_1, Z_2, Z_3, …, Z_6, with a spacing of 15 mm. The thickness of the filled particles in the chute is 110 mm. The diameter of the filled particles is 10 mm, and the diameter of the spherical detector is 30 mm. To ensure that the velocity of the bottom particle is 0, a rough surface with a coefficient of friction of 0.8 is set as the bottom of the chute. More detailed description of the system is given in Refs. [14,15].

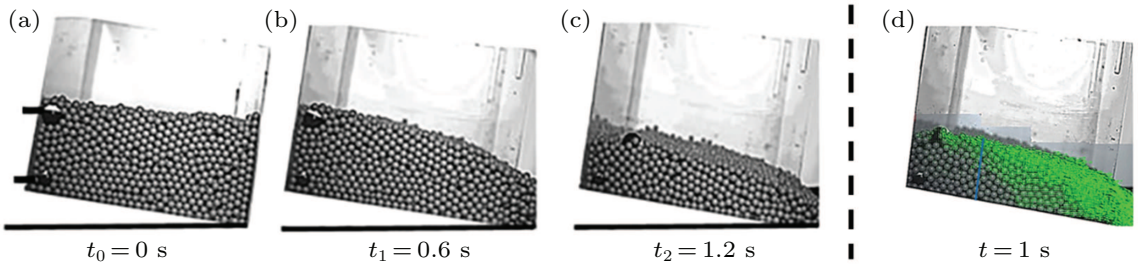


Fig. 2. Snapshots of chute granular flow, showing granular profile at (a) $t_0 = 0$, (b) $t_1 = 0.6$ s, chute granular flow formed stable local flow velocity distribution; (c) after $t_2 = 1.2$ s, local flow velocity distribution failing to be maintained due to the inadequate thickness of the particle bed in the chute; (d) example displaying the granular flow at $t = 1$ s to show the PIV measurement results.

2.2. Spherical detector based on embedded inertial navigation technology

The spherical detector is used to measure the angular velocity, acceleration and other movement data during the experiment through using embedded inertial navigation technology.

Any attitude in three-dimensional space can be represented concisely, intuitively by Euler angles. The aerial sequential Euler angles (shown in Fig. 3(a)) are used to represent the attitude of spherical detectors, φ, χ, Ψ, respectively, as the roll angle, pitch angle, and yaw angle. In the carrier coordinate system of the spherical detector, x_b moves to the right along the horizontal axis, y_b moves forward along the longitudinal axis, and z_b moves along the vertical axis. In the spatial coordinate system (E), x_E is the projection of x_b on the horizontal plane, y_E is perpendicular to x_E, and z_E is perpendicular to the horizontal plane.

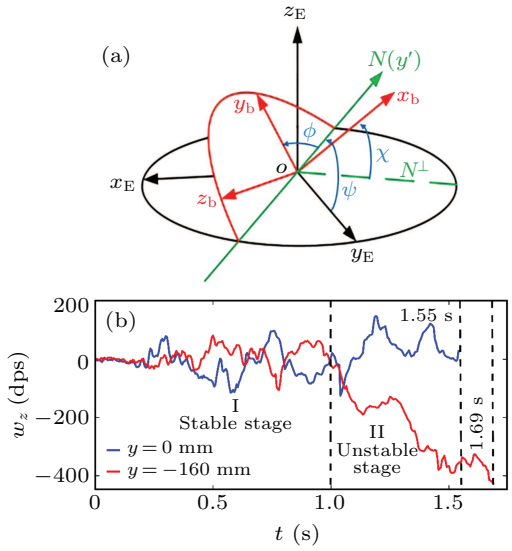


Fig. 3. (a) Schematic diagram of attitude angle of spherical detector, with ω_x', ω_y', ω_z', respectively, representing the components of original angular velocity of rolling around the x axis, y axis, and z axis, and ω_y being the angular velocity of rolling around the y axis; (b) results from a typical experiment with two detectors placed side by side at Z_1.[14,15]

The Euler angle is adopted in the measurement system to represent the attitude, and a quaternion is used to represent the attitude when it is solved.[25,26] The attitude update equation of the inertial measurement unit (ω_x, ω_y, and ω_z are the values that are measured by the gyroscope) is given as follows:

$$q(k) = \left(N + \frac{1}{2}\Omega_{nb}^{n} T\right) q(k-1), \tag{2}$$

$$\Omega_{nb}^{n} = \begin{bmatrix} 0 & -\omega_x & -\omega_y & -\omega_z \\ \omega_x & 0 & \omega_z & -\omega_y \\ \omega_y & -\omega_z & 0 & \omega_x \\ \omega_z & \omega_y & -\omega_x & 0 \end{bmatrix}, \tag{3}$$

where q is the quaternion expression. N is the unit matrix, Ω_{nb}^{n} is the skew matrix of angular velocity, and T is the time interval.

Therefore, the attitude of the spherical detector is converted into a quaternion representation through the following equation during the attitude solution:

$$q = \begin{bmatrix} q_0 \\ q_1 \\ q_2 \\ q_3 \end{bmatrix} = \begin{bmatrix} \cos\left(\frac{\psi}{2}\right)\cos\left(\frac{\chi}{2}\right)\cos\left(\frac{\varphi}{2}\right) + \sin\left(\frac{\psi}{2}\right)\sin\left(\frac{\chi}{2}\right)\sin\left(\frac{\varphi}{2}\right) \\ \cos\left(\frac{\psi}{2}\right)\cos\left(\frac{\chi}{2}\right)\sin\left(\frac{\varphi}{2}\right) - \sin\left(\frac{\psi}{2}\right)\sin\left(\frac{\chi}{2}\right)\cos\left(\frac{\varphi}{2}\right) \\ \cos\left(\frac{\psi}{2}\right)\sin\left(\frac{\chi}{2}\right)\cos\left(\frac{\varphi}{2}\right) + \sin\left(\frac{\psi}{2}\right)\cos\left(\frac{\chi}{2}\right)\sin\left(\frac{\varphi}{2}\right) \\ \sin\left(\frac{\psi}{2}\right)\cos\left(\frac{\chi}{2}\right)\cos\left(\frac{\varphi}{2}\right) - \cos\left(\frac{\psi}{2}\right)\sin\left(\frac{\chi}{2}\right)\sin\left(\frac{\varphi}{2}\right) \end{bmatrix}. \tag{4}$$

After the attitude solution is completed, the attitude is converted into Euler angles throughthe following equation:

$$\begin{bmatrix} \psi \\ \theta \\ \varphi \end{bmatrix} = \begin{bmatrix} \arctan 2\left(2\left(q_0 q_3 + q_1 q_2\right), 1 - 2\left(q_0^2 + q_1^2\right)\right) \\ \arcsin\left(2\left(q_1 q_3 - q_0 q_2\right)\right) \\ \arctan 2\left(2\left(q_2 q_3 + q_0 q_1\right), 1 - 2\left(q_1^2 + q_2^2\right)\right) \end{bmatrix}. \tag{5}$$

Through multiple experiments, the experimental results of spherical particle wireless measurement technology based on inertial navigation technology are validated and can be used to measure the angular velocity and translational velocity of particles in the chute system.[15,18]

Figure 3(b) shows a typical experimental results obtained by using two spherical detectors placed at Z_1. It can be found that the movement process of the detectors can be divided into stable stage and unstable stage by the rotating speed.[14] To discuss the rolling and sliding of the detector, we focus on the relationship between the particle flow velocity distribution and the special tracer particle velocity characteristic from 0.6 s to 1 s (stable stage).

2.3. DEM simulation

2.3.1. DEM contact model

The most important step in DEM is to choose a reasonable physical contact model. The model of Hertz–Mindlin (no slip) with RVD rolling friction adjusts the calculation method of rolling friction to ensure that three dimensions have the proper functionality without affecting the calculation time. It is especially suitable for strong rotation systems that have strict requirements for particle rotation characteristics.[24] Therefore, in this paper DEM is used based on the model of the Hertz–Mindlin (no slip) with RVD rolling friction contact to simulate the discharge process of spherical particles in a chute. According to the relative rotational velocity between contact particles, the particle rolling friction is calculated as follows:[27]

$$\begin{cases} \boldsymbol{\tau} = -\mu_r F_n R^* \hat{\omega}_{rel}, \\ F_n = \dfrac{4}{3} E^* \sqrt{R^*}\, \delta_n^{3/2}, \end{cases} \tag{6}$$

where torque $\boldsymbol{\tau}$ represents the rolling friction of the particles, μ_r is the rolling friction coefficient, F_n is the normal force between particles, R^* is the equivalent radius between particles, $\hat{\omega}_{rel}$ is the unit vector of relative rotational velocity, E^* is the equivalent Young's modulus, and δ_n is the normal overlap amount.

The equivalent radius R^* and the equivalent Young's modulus E^* are calculated from the following equations:

$$\begin{cases} \dfrac{1}{R^*} = \dfrac{1}{R_i} + \dfrac{1}{R_j}, \\ \dfrac{1}{E^*} = \dfrac{(1-v_i^2)}{E_i} + \dfrac{(1-v_j^2)}{E_j}, \end{cases} \tag{7}$$

where i and j represent the two particles in contact, R_i and R_j are the radii of the contact particles, v_i and v_j are the Poisson's ratio, E_i and E_j are the Young's moduli.

2.3.2. Simulation setup

Figure 4(a) shows the theoretical model of chute flow defined three layers based on the velocity distribution.[28] The experimental results presented in Ref. [15] indicate that the rolling contribution rate is an important factor affecting velocity composition. Figure 4(b) shows the simulation chute cross-sectional surface sliced into 30×60 grids, and each grid is the smallest statistical unit with a size of 10 mm×20 mm×10 mm. In the simulation, the average movement information of the particles in each grid is used. The simulation process is the same as the experimental process shown in Fig. 2. Three particles ($d = 1$ cm) in each layer are marked. A detector ($d = 3$ cm) is placed in the granular bed at Z point, near particle B.

During the simulation, the time interval for collecting particle motion data is set to be 0.01 s. In order to ensure the stability of experiment, the minimum time step in experiment is set to be 2.71×10^{-5} s, which is less than the Rayleigh time of particle 5.82×10^{-5} s.[29] Other system parameters of DEM simulation are shown in Table 1.

Among them, the friction coefficient between particles $\mu_{\mathrm{p-p}}$ is obtained by measuring the repose angle of particle accumulation, and the coefficient of restitution e is obtained by the particle rebound experiment.[30]

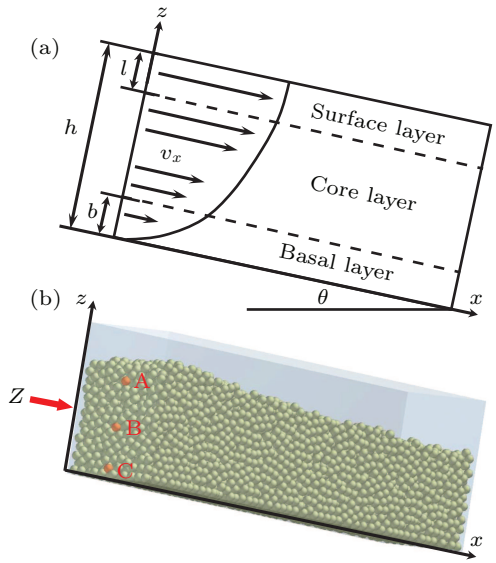


Fig. 4. Simulation based on the velocity layers: (a) schematic model of the chute system and (b) geometry of chute with an initial packed bed.

Table 1. Physical parameters employed in experiments and simulations.

		Parameter	Symbol	Value
Simulation	particle	density	ρ (kg·m^{-3})	1400
		Young's modulus	E_{p} (Pa)	2.835×10^{9}
		Poisson's ratio	ν	0.35
	wall	density	ρ (kg·m^{-3})	1180
		Young's modulus	E_{p} (Pa)	4.76×10^{9}
		Poisson's ratio	ν	0.4
	particle-particle interaction	static friction coefficient	$\mu_{\mathrm{p-p}}$	0.6
		rolling friction coefficient	$\mu_{\mathrm{r\ p-p}}$	4.2×10^{-5}
		restitution coefficient	e_{p}	0.87
	particle-wall interaction	static friction coefficient	$\mu_{\mathrm{p-w}}$	0.6
		rolling friction coefficient	$\mu_{\mathrm{r\ p-w}}$	27.1×10^{-5}
		restitution coefficient	e_{w}	0.88
Experiment	particle	density	ρ (kg·m^{-3})	1400
		Young's modulus	E_{p} (Pa)	–
		Poisson's ratio	ν	–
	wall	density	ρ (kg·m^{-3})	1400
		Young's modulus	E_{p} (Pa)	–
		Poisson's ratio	ν	–
	bottom	static friction coefficient	μ_{b}	0.8
	particle-particle interaction	static friction coefficient	$\mu_{\mathrm{p-p}}$	0.6
		rolling friction coefficient	$\mu_{\mathrm{r\ p-p}}$	–
		restitution coefficient	$\mathrm{e_p}$	0.87
	particle-wall interaction	static friction coefficient	$\mu_{\mathrm{p-w}}$	0.6
		rolling friction coefficient	$\mu_{\mathrm{r\ p-w}}$	–
		restitution coefficient	e_{w}	0.88

3. Results and discussion

3.1. Relative motion between detector and granular flow

In the local granular flow model, it is believed that the flow velocity $v_x(z)$ is positively correlated with $z^{3/2}$. The relationship between the flow velocity and the height of the chute can be expressed as (also known as Silbert's formula)[7]

$$v(z) = I(\tan\theta)\frac{2}{3}\frac{\sqrt{\rho g\cos\theta}}{d}h^{3/2}\left[1-\left(\frac{h-z}{h}\right)^{3/2}\right], \quad (8)$$

where I is the inertial number which increases with inclination angle θ, increasing, h is the thickness of the filling particle, ρ is the density of the filling particle, g is the acceleration of gravity, θ is the angle between the chute and the ground, and z is the height of the chute. Based on Eq. (8), the calculated velocity of the granular flow is shown by the red line in Fig. 5(a) when θ is 12°.

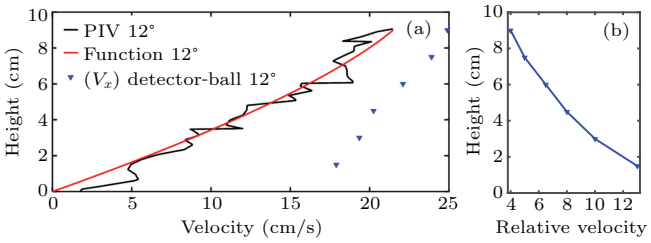


Fig. 5. (a) Comparison between theoretical curve and experimental curve of, chute height *versus* particle flow velocity, with red line representing velocity based on Eq. (8), where $I = 0.178$, black line denoting averaged velocity measured by PIV method. and blue triangles referring to the velocities measured by using a spherical detector at six marked locations; and (b) curve of chute height *versus* relative velocity between the detector and the granular flow.

We use the PIV method to obtain the averaged velocity profile on the side wall of the chute, and the detector to obtain the average velocity of special tracer particle during the stable period. It is shown in Fig. 5(a) that the averaged velocity measured by the PIV method is similar to that obtained from the theoretical model, Eq. (8). The red line shows that the granular velocity at the bottom is not 0, whereas in Eq. (8) the grain at the bottom should not slip. This is because the chute does not use particle bed as bottom, so the granular layer at the bottom does not form complete stable state.

The velocity measured by the detector at different values of h (as shown by the blue points) is larger than the PIV results and increases linearly. This indicates that the detector moves faster than the surrounding particles. The relative velocity between the detector and the granular flow is shown by Fig. 5(b). The biggest difference in velocity appears at the bottom.

3.2. Rolling velocity and sliding velocity

During the experiment, it can be observed in Fig. 2 that the particles in the chute have not only sliding motion, but also rolling motion. The velocity of the spherical detector is a combination of sliding velocity and rolling velocity as shown in Fig. 6.

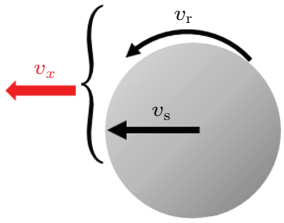


Fig. 6. Composition of velocity: sliding velocity v_s and rolling velocity v_r.

The velocity along the flow direction $v_x(z)$ of the spherical detector can be expressed as

$$v_x(z) = v_s(z) + v_r(z), \tag{9}$$

where $v_s(z)$ is the sliding velocity and $v_r(z)$ is the rolling velocity.

The rolling velocity $v_r(z)$ can be calculated from

$$v_r(z) = \overline{\omega_y}(z) \cdot R, \tag{10}$$

where $\overline{\omega_y}(z)$ is the average angular velocity of the spherical detector around the Y axis, and R is the radius of the spherical detector. Figure 7 shows the averaged angular velocity $\overline{\omega_y}(z)$ of particles for different values of inclination chute angle, θ, of 8°/10°/12°, respectively.

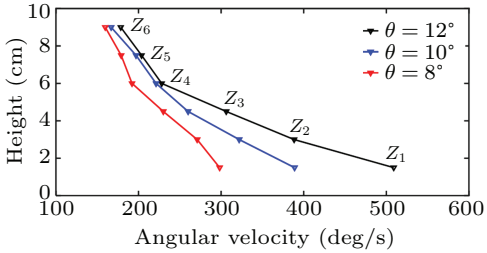


Fig. 7. Curves of chute height *versus* averaged angular velocity $\overline{\omega_y}(z)$ of the spherical detector at different inclination angles.

Figure 7 shows that the chute height decreases with average rolling angular velocity $\overline{\omega_y}(z)$ increasing for all inclination angles. The increasing of the inclination angle of the chute will increase $\overline{\omega_y}(z)$. At the bottom of the chute, the variation of θ has a greater influence on the average rolling angular velocity $\overline{\omega_y}(z)$. On the free surface, the effect of θ is minimal.

$$v_s'(z) = v_x(z) - v_r(z). \tag{11}$$

After obtaining $\overline{\omega_y}(z)$, the sliding velocity v_s' of particle is obtained according to Eqs. (10) and (11). The magnitudes of sliding velocity $v_s'(z)$ of particles at different inclination angles are compared with the calculated results from Eq. (8).

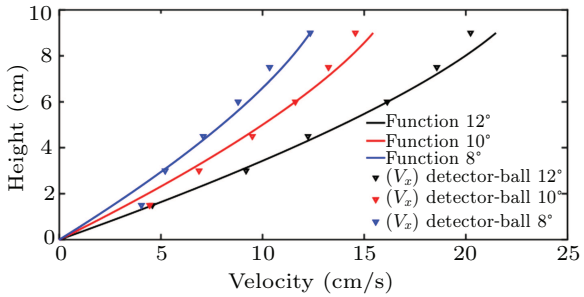


Fig. 8. Comparison of particle sliding velocity $v_s(z)$ among different values of inclination angle θ, with solid lines representing velocities calculated from Eq. (8), triangles denoting velocities measured by the spherical detector. Inertial number $I = 0.178$ when $\theta = 12°$, $I = 0.140$ when $\theta = 10°$. $I = 0.125$ when $\theta = 8°$.

As shown in Fig. 8, the sliding velocities measured by detector and calculated from Eq. (8) are matched. At the free

surface of the chute, the growth pattern of particle sliding velocity $v_s(z)$ tends to be flat. This is one of the characteristics of the local flow model, indicating that the sliding velocity of the detector is mainly driven by the local granular flow. Correspondingly, the velocity of the detector relative to the surrounding particles is mainly due to rolling.

3.3. Relative motion based on simulation results

Using the detector and PIV technology, the measurement results show that rolling and relative motion are statistically correlated. For further investigation, the results obtained from the DEM simulation (Fig. 4) are analyzed. The area in the middle of the chute is considered as the area that contains valid granular flow velocity distribution as shown in the inset of Fig. 9. The velocities of each particle are shown by the black triangles. Calculations from Eq. (8) are shown by the red line. It can be observed that the simulation results are in line with the experimental results as shown by the blue line (the same as the red line in Fig. 5). The slight difference in I between 0.178 in experiment result and 0.182 in simulation result may be due to the ideal shear process obtained by simulation.

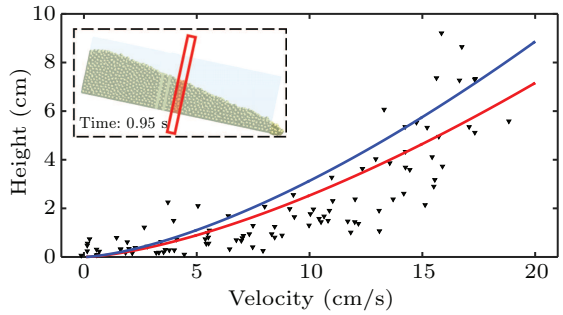


Fig. 9. Simulated velocity distributions, with inset showing measured area, triangles representing velocities of particles in measured area, red line ($I = 0.182$) and blue line ($I = 0.178$) denoting calculations from Eq. (8) based on the simulation and the experimental results.

By tracking the labeled particles, simulation results provide the accurate trajectories and real-time rolling velocities that cannot be obtained experimentally.

Figure 10(a) shows the rolling velocities of 3 labeled particles. The rolling velocity of particle A is larger than those of the other two labeled particles. The velocity v_x of particle A located in the surface layer (Fig. 4) is significantly higher than those in the other layers. It takes less than 2 s to move out of the chute. This is consistent with the theory presented in Subsection 3.1.

The velocity ω_y of particle B is slightly larger than that of particle C in the stable stage. After 1.5 s, the values of ω_y of particles B and C are the same. By tracking the labeled particles, it is found that particle B falls in height as it follows granular flow and approaches to particle C in a time between 0.5 s and 1.5 s. This causes relative motion between particle B and the core layer. After 1.5 s, particles B and C follow similar trajectories moving out of the chute. So a similar ω_y is obtained.

Because of the difference in v_x, the particles in different layers have obvious relative motions. The relative motion trajectory is consistent with that of velocity ω_y.

Figure 10(b) shows time-dependent ω_y of the detector and particle B. The detector moves faster, leaving the chute 0.55 s earlier than particle B at a similar initial position. Comparing with ω_y in the moving duration, the rotation of the detector is more stable and larger than the particle B on average. Several larger pulses in red line indicate that particle B moves intensely when there is a gap.

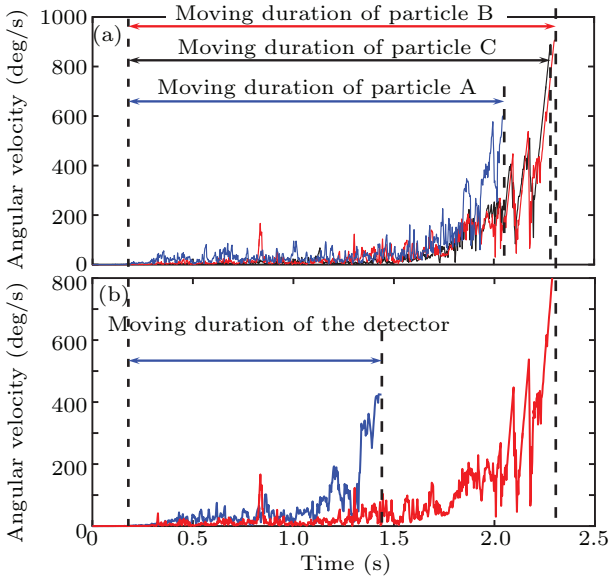


Fig. 10. (a) Curve of time-dependent angular velocity ω_y of particles A (blue line), B (red line), and C (black line) on surface, core, and basal layer. (b) Curve of time-dependent angular velocity ω_y of detector (blue line) and particle B (red line) located at similar initial position.

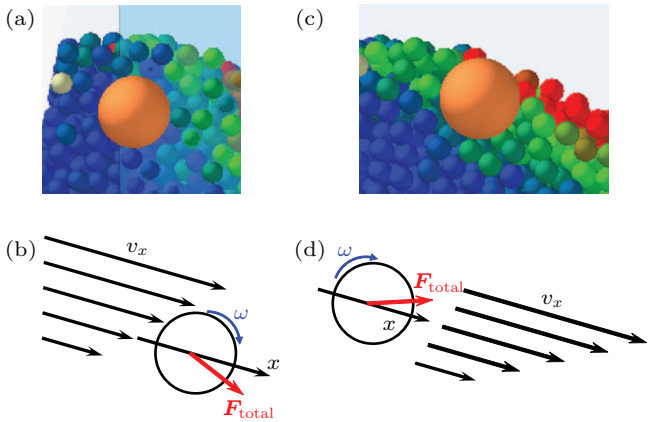


Fig. 11. Two potential mechanisms of ω_y of detector: (a) detector surrounded by granular flow; (b) detector driven by the unbalanced granular flow; (c) detector starting to surface the granular flow; (d) detector driven by gravity.

Based on the ω_y, two potential mechanisms of the detector rolling are presented in Fig. 11. During the stable stage, the detector is surrounded by the granular flow as shown in Fig. 11(a). Because of the difference in v_x at different val-

ues of h, the detector rolls forward under the drive unbalanced granular flow as shown in Fig. 11(b).

During the unstable stage, the upper part of the detector is not covered by the granular flow. Figure 11(c) shows the moment when the detector surfaces the granular flow. It can be observed that v_x below the detector is not uniform. At this stage, the detector is driven by gravity, moving to the region with higher v_x.

Further investigation of the detector trajectory shows that the mechanism of ω_y of the detector is correlated with the layer at which the detector is located. In the surface and basal layer, the detector has a higher probability of moving upwards. The direction is similar to that shown in Fig. 11(d). In the core layer, the trajectory of the detector is very complex. The motion directions indicated by both mechanisms occur. The relationship between rolling mechanism and time-space will be the focus of further research.

4. Conclusions

We experimentally studied a special particle moving in the local granular flow and consider that the velocity of the special particle should be divided into sliding velocity $v_{\mathrm{s}}(z)$ and rolling velocity $v_{\mathrm{r}}(z)$. As h increases, the sliding velocity $v_{\mathrm{s}}(z)$ of particles increases, but rolling velocity $v_{\mathrm{r}}(z)$ decreases. The velocity $v_x(z)$ of particles presents a linear growth, and $\overline{\omega_y}(z)$ can be obtained by a spherical detector, thus the rolling velocity of the particle $v_{\mathrm{r}}(z)$ can be obtained. Two potential mechanisms of ω_y are presented based on the DEM simulation with RVD rolling friction model, and ω_y of the detector changes in different flow stages and layers. In further studies, the relationship between mechanism of ω_y and time-space of the detector needs to be analyzed precisely and compared with theoretical models.

Acknowledgements

We would like to express our gratitude to Prof. V. Zivkovic from Newcastle University for his careful guidance and help.

Project supported by the National Natural Science Foundation of China (Grant Nos. 11972212, 12072200, and 12002213).

References

[1] Zhang S, Wei K, Xiao Y, Ma X H, Zhang Y C, Liu G G, Lei T M, Zheng Y K, Huang S, Wang N, Asif M and Liu X Y 2018 *Chin. Phys. B* **27** 097309
[2] Louge M Y and Keast S C 2001 *Phys. Fluids* **13** 1213
[3] Lemieux P A and Durian D J 2000 *Phys. Rev. Lett.* **85** 4273
[4] Zheng Q J, Bai L, Yang L and Yu A B 2019 *Ind. Eng. Chem. Res.* **58** 19251
[5] Umbanhowar P B, Lueptow R M and Ottino J M 2019 *Annu. Rev. Chem. Biom. Eng.* **10** 11
[6] Pouliquen O and Forterre Y 2002 *J. Fluid Mech.* **453** 133
[7] Pouliquen O and Forterre Y 2009 *Philos. Trans. Royal Soc. A* **367** 5091
[8] Jop P, Forterre Y and Pouliquen O 2006 *Nature* **441** 727
[9] Midi G 2004 *Eur. Phys. J. E* **14** 341
[10] Cruz F D, Emam S, Prochnow M, Roux J N and Chevoir F 2005 *Phys. Rev. E* **72** 021309
[11] Forterre Y and Pouliquen O 2011 *Glass and Grains* **61** 77
[12] Tripathi A and Khakhar D V 2011 *Phys. Fluids* **23** 147
[13] Halsey T C 2009 *Phys. Rev. E* **80** 011303
[14] Wang R, Li R, Wang S S, Chen Q and Yang H 2021 *Particuology* **54** 102
[15] Wang S S, Li R, Chen Q, Zheng G, Zivkovic V and Yang H 2020 *Powder Technol.* **376** 22
[16] Caviezel A, Schaffner M, Cavigelli L, Buhler Y, Bartelt P and Magno M 2018 *IEEE Trans. Instrum. Meas.* **67** 1
[17] Caviezel A, Demmel S E, Ringenbach A, Buhler Y, Lu G, Christen M, Dinneen C E, Eberhard L A, Rickenbach D V and Bartelt P 2019 *Earth Surf. Dynam.* **7** 199
[18] Zhu Y H, Yang H, Li R, Zhang Y J, Chen Q, Hua Y S, Sun Q C and Kong P 2020 *Powder Technol.* **360** 882
[19] Yang H, Zhang G, Wang Y and Sun Q C 2018 *Adv. Mech.* **48** 541
[20] Dong Y X, Zhang G H, Sun Q C, Zhao X D and Niu X N 2015 *Chin. Phys. Lett.* **32** 126201
[21] Song Z B, Yang X Y, Feng W X, Xi Z H, Li L J and Shi Y R 2018 *Chin. Phys. B* **27** 074501
[22] Feng Y and Yuan Z R 2021 *Comput. Part. Mech.* **8** 21
[23] Yu Y W and Saxen H 2011 *Adv. Powder Technol.* **22** 324
[24] Tripathi A, Kumar V, Agarwal A, Tripathi A, Basu S, Chakrabarty A and Nag S 2021 *Powder Technol.* **380** 288
[25] Ozdemir M and Ergin A A 2006 *J. Geom. Phys.* **56** 322
[26] Sabatelli S, Galgani M, Fanucci L and Rocchi A 2013 *IEEE Trans. Instrum. Meas.* **62** 590
[27] Ai J, Chen J F, Rotter J M and Ooi J Y 2011 *Powder Technol.* **206** 269
[28] Silbert L E, Ertas D, Grest G S, Halsey T C, Levine D and Plimpton S J 2001 *Phys. Rev. E* **64** 051302
[29] Washino K, Chan E L, Miyazaki K, Tsuji T and Tanaka T 2016 *Powder Technol.* **302** 100
[30] Höhner D, Wirtz S and Scherer V 2013 *Powder Technol.* **235** 614